Journal of Power Sources 241 (2013) 295–310

Contents lists available at SciVerse ScienceDirect

Journal of Power Sources

journal homepage: www.elsevier.com/locate/jpowsour

A new extension of physics-based single particle model for higher charge–discharge rates

Weilin Luo, Chao Lyu*, Lixin Wang, Liqiang Zhang

School of Electrical Engineering and Automation, Harbin Institute of Technology, No. 92, West Dazhi Street, Nangang District, Harbin 150001, Heilongjiang, PR China

HIGHLIGHTS

- The non-uniform reaction distribution effect is extended into single particle model.
- New model can accurately predict the pore wall flux distribution inside the electrode.
- New model can be used for higher charge–discharge rates up to 4C with a good accuracy.
- New model can be applied to the dynamic loads in EV and HEV applications.
- New model is a lumped-parameter analytical model with a good computational efficiency.

ARTICLE INFO

Article history:
Received 11 March 2013
Accepted 26 April 2013
Available online 4 May 2013

Keywords:
Lithium ion battery
Physics based model
Model order reduction
Model simplification
Single particle model
Extended single particle model

ABSTRACT

A new approximate physics-based Lithium-ion cell model is developed by extending the descriptions of the non-uniform reaction distribution effect and the electrolyte concentration/potential distribution effect into single particle model, namely the extended single particle model. In this model, the simplification of the solid-phase diffusion is based on the existing approximate solution where a polynomial is used to approximate the concentration profile inside the particle. Diffusion in the electrolyte and the concentration polarization effect are simplified using the approximate solution based on parabolic profile approximation for the electrolyte concentration distribution. Especially, this model analyzes the mathematical description of the non-uniform reaction distribution effect inside the electrode, and an approximate solution of this effect is obtained by synthetically applying the volume average technique, approximated by the uniform reaction distribution situation, exponential profile approximation and the iterative calculation techniques. Thus the description of the non-uniform reaction distribution effect is successfully extended and the pore wall fluxes at the two current collector interfaces can be accurately predicted. Simulation results show that this model greatly improves the computational efficiency with little loss of accuracy.

© 2013 Elsevier B.V. All rights reserved.

1. Introduction

Lithium-ion batteries have been chosen as power suppliers for many systems due to their various advantages [1]. Obtaining an accurate mathematical model to describe the working and aging behaviors of the battery is the key to the research on battery reliability including issues such as battery health assessment, state of charge estimation, state of health estimation and remaining useful life prediction. Up to now, mathematical models of lithium-ion batteries' working dynamics have been investigated and used in the cell design, especially the pseudo 2D model (P2D), which is based on the theories of porous electrodes and concentrated solutions [2], and which describes the microcosmic behavior of the lithium ions inside the cell with the first principles-based derivation of the governing equations. These physics-based models have been used by various researchers to optimize the cell design and to study the effect of system parameters and thermal behavior [3]. Comparing to various experiential equivalent circuit models, the physics-based model can capture the electrochemical reaction dynamics and predict the batteries' behavior under any type of operating conditions with better accuracy.

Unfortunately, however, the rigorous physics-based model needs a high computational requirement due to its complex coupled nonlinear partial differential equations (PDEs). This characteristic limits its application such as real time control, on-line

* Corresponding author. Tel.: +86 18646386016; fax: +86 451 86402965.
E-mail addresses: luoweilin@hit.edu.cn (W. Luo), lu_chao@hit.edu.cn (C. Lyu), wlx@hit.edu.cn (L. Wang), zhang.lq@foxmail.com (L. Zhang).

0378-7753/$ – see front matter © 2013 Elsevier B.V. All rights reserved.
http://dx.doi.org/10.1016/j.jpowsour.2013.04.129

estimation and prediction embedded in a microprocessor. Therefore, it is important to simplify or reformulate the rigorous physics-based model, to explore analytical or approximate solutions for the model, and to seek the reduced order models to improve the computational efficiency. The goal of current work is to establish an approximate physics-based lithium-ion cell model which can be solvable real time with a normal computing requirement and can predict the behaviors of batteries with little loss of accuracy.

Many efforts have explored methodologies to update the original physics-based models in order to make them simpler and more computationally efficient like proper orthogonal decomposition (POD), Liapunov–Schmidt technique, the combination of coordinate transformation and orthogonal collocation, etc. [4–10]. These methods based on the mathematical techniques have their own limitations. For example POD-based techniques use the full numerical solution to fit a reduced set of eigen-values and nodes to get a meaningful solution with a reduced number of equations. However, this method requires rigorous numerical solutions to build the POD reduced-order models. Also, once the operating condition is changed, the boundary conditions are modified, or if the parameter values are adjusted significantly, the POD model needs to be reconstructed [8]. Subramanian et al. focus on the reformulation of the rigorous model toward real-time (milliseconds) simulation and parameter estimation, the reformulated model developed by them results in fewer differential algebraic equations (DAEs) which allows for easier and quicker computation compared with the traditional finite difference approach [7]. This method decreases the number of DAEs, but the complexity of each DAE increases, and the computational resources required for the system is still not ideal for the real-time simulation embedded in a microprocessor.

The single particle (SP) model is an existing approximate physics-based model. SP model considers all the reactions inside the electrode as distributed uniformly over all the particles, ignoring the variation of electrolyte concentration and potential with position and time. Due to this key assumption, SP model can be quickly simulated, but is only valid for limited conditions, such as low rates and thin electrodes [4]. As for dynamic operating conditions such as Federal Urban Driving Schedule and some conditions with high-rate charge–discharge pulses, SP model is no longer valid.

Analyzing current researches on this issue, the authors believe that various mathematical techniques can be applied here, but the ultimate cause of the complexity roots in the nature of the model. Based on this notion, this paper focuses on exploiting the essential chemical and physical processes which characterize the behavior of the cell, the dominating essential process being found to be non-uniform reaction distribution effect inside the porous electrode. In addition, this effect is discovered to be the key reason why SP model is not valid for higher charge–discharge rates. Then, this paper presents the mathematical description of the non-uniform reaction distribution effect and develops an approximate solution to compute this effect. Based on this approximate solution for the non-uniform reaction distribution effect and the approximate solution for the electrolyte concentration distribution proposed by the authors before [11], SP model is extended. This new approximate physics-based model is named as extended single particle (ESP) model. Compared with SP model, ESP model extends the descriptions of the non-uniform reaction distribution effect and the electrolyte concentration/potential distribution effect; therefore, it improves the model prediction quality. Meanwhile, ESP model is derived from the analysis of the essential physical processes, which guarantees the accuracy and the availability under various operating conditions. In addition, ESP model describes the dynamics with analytical functions, decreases the computational requirement fundamentally, and, therefore, it can provide higher computational efficiency.

The remainder of this paper is organized as follows. In Section 2, the rigorous physics-based model (i.e. the P2D model) and the SP model are analyzed. In Section 3, the non-uniform reaction distribution effect and its mathematical description are presented. Then, the approximate solution of the non-uniform reaction distribution effect is derived. Lastly, the computation of the overpotentials and the terminal voltage are presented. ESP model is established. The validation of ESP model and its comparison with SP and P2D models are discussed in Section 4, followed by conclusions presented in Section 5.

2. State-of-the-art physics-based modeling

2.1. The rigorous physics-based model

As illustrated in Fig. 1, the lithium-ion cell consists of a negative electrode, a micro porous separator, a positive electrode and two current collectors at the ends of the two electrodes. Typically, both electrodes consist of a grain structure of quasi-spheric active particles in a μm scale. The lithium ions are transported by diffusion inside the active particles along the r-axis, which is called solid-phase diffusion process. The concentrations of ions at the surface of the active particles determine the potentials at different positions of the electrodes, and the difference in the potentials at the two interfaces between the current collectors and the electrodes determines the terminal voltage of the cell. The interspaces between the particles are filled with electrolyte. The electrochemical reactions take place at the interfaces between the particles and the electrolyte according to the Butler–Volmer kinetics. The electrons are transported to the current collectors, and the lithium ions carrying the charge travel via diffusion and migration in the electrolyte through the separator to the other electrode along the x-axis, as shown in Fig. 1. A detailed discussion on the principle of lithium-ion cell can be found in Ref. [12] for instance.

The rigorous physics-based full order Li-ion cell model is proposed by Newman and Doyle et al. [13], which is named as P2D model. Based on the theories of porous electrodes and concentrated solutions, P2D model mainly consists of ten coupled nonlinear PDEs, which describe the solid-phase diffusion within the particles, the diffusion in the electrolyte, the balance of the solid-phase potential and the electrolyte potential occurring in the three regions in a lithium-ion cell. The model typically gives solutions to the electrolyte concentration, electrolyte potential, solid-phase potential, and solid-phase concentration in the negative and positive electrodes and the electrolyte concentration and electrolyte potential in the separator [14]. The details of P2D model are given in Tables 1 and 2, and the parameters used in this study are given in Table 3.

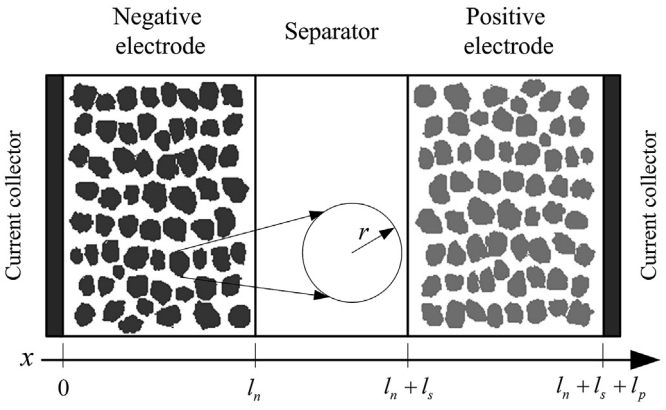

Fig. 1. Schematic representation of a lithium-ion dual intercalation cell [2].

Table 1
Governing equations of the P2D lithium-ion cell model [7].

Governing equations	Boundary conditions
Negative electrode	
$\varepsilon_n \frac{\partial c}{\partial t} = D_{\text{eff},n}\frac{\partial^2 c}{\partial x^2} + a_n(1-t_+)j_n$	$\left.\frac{\partial c}{\partial x}\right\|_{x=0} = 0,\ -D_{\text{eff},n}\left.\frac{\partial c}{\partial x}\right\|_{x=l_n^-} = -D_{\text{eff},s}\left.\frac{\partial c}{\partial x}\right\|_{x=l_n^+}$ (1)
$-\sigma_{\text{eff},n}\frac{\partial \Phi_1}{\partial x} - \kappa_{\text{eff},n}\frac{\partial \Phi_2}{\partial x} + 2\frac{\kappa_{\text{eff},n}RT}{F}(1-t_+)\frac{\partial \ln c}{\partial x} = I$	$\left.\frac{\partial \Phi_2}{\partial x}\right\|_{x=0} = 0,\ -\kappa_{\text{eff},n}\left.\frac{\partial \Phi_2}{\partial x}\right\|_{x=l_n^-} = -\kappa_{\text{eff},s}\left.\frac{\partial \Phi_2}{\partial x}\right\|_{x=l_n^+}$ (2)
$\sigma_{\text{eff},n}\frac{\partial^2 \Phi_1}{\partial x^2} = a_n F j_n$	$-\sigma_{\text{eff},n}\left.\frac{\partial \Phi_1}{\partial x}\right\|_{x=0} = I,\ \left.\frac{\partial \Phi_1}{\partial x}\right\|_{x=l_n} = 0$ (3)
$\frac{\partial c_n^s}{\partial t} = D_{s,n}\frac{1}{r^2}\frac{\partial}{\partial r}\left(r^2\frac{\partial c_n^s}{\partial r}\right)$	$\left.\frac{\partial c_n^s}{\partial r}\right\|_{r=0} = 0,\ D_{s,n}\left.\frac{\partial c_n^s}{\partial r}\right\|_{r=R_n} = -j_n$ (4)
Separator	
$\varepsilon_s \frac{\partial c}{\partial t} = D_{\text{eff},s}\frac{\partial^2 c}{\partial x^2}$	$-D_{\text{eff},s}\left.\frac{\partial c}{\partial x}\right\|_{x=(l_n+l_s)^-} = -D_{\text{eff},p}\left.\frac{\partial c}{\partial x}\right\|_{x=(l_n+l_s)^+}$ (5)
	$c\|_{x=l_n^-} = c\|_{x=l_n^+},\ c\|_{x=(l_n+l_s)^-} = c\|_{x=(l_n+l_s)^+}$
$-\kappa_{\text{eff},s}\frac{\partial \Phi_2}{\partial x} + 2\frac{\kappa_{\text{eff},s}RT}{F}(1-t_+)\frac{\partial \ln c}{\partial x} = I$	$-\kappa_{\text{eff},s}\left.\frac{\partial \Phi_2}{\partial x}\right\|_{x=(l_n+l_s)^-} = -\kappa_{\text{eff},p}\left.\frac{\partial \Phi_2}{\partial x}\right\|_{x=(l_n+l_s)^+}$ (6)
	$\Phi_2\|_{x=l_n^-} = \Phi_2\|_{x=l_n^+},\ \Phi_2\|_{x=(l_n+l_s)^-} = \Phi_2\|_{x=(l_n+l_s)^+}$
Positive electrode	
$\varepsilon_p \frac{\partial c}{\partial t} = D_{\text{eff},p}\frac{\partial^2 c}{\partial x^2} + a_p(1-t_+)j_p$	$\left.\frac{\partial c}{\partial x}\right\|_{x=l_n+l_s+l_p} = 0$ (7)
$-\sigma_{\text{eff},p}\frac{\partial \Phi_1}{\partial x} - \kappa_{\text{eff},p}\frac{\partial \Phi_2}{\partial x} + 2\frac{\kappa_{\text{eff},p}RT}{F}(1-t_+)\frac{\partial \ln c}{\partial x} = I$	$\Phi_2\|_{x=l_n+l_s+l_p} = 0$ (8)
$\sigma_{\text{eff},p}\frac{\partial^2 \Phi_1}{\partial x^2} = a_p F j_p$	$-\sigma_{\text{eff},p}\left.\frac{\partial \Phi_1}{\partial x}\right\|_{x=l_n+l_s+l_p} = I,\ \left.\frac{\partial \Phi_1}{\partial x}\right\|_{x=l_n+l_s} = 0$ (9)
$\frac{\partial c_p^s}{\partial t} = D_{s,p}\frac{1}{r^2}\frac{\partial}{\partial r}\left(r^2\frac{\partial c_p^s}{\partial r}\right)$	$\left.\frac{\partial c_p^s}{\partial r}\right\|_{r=0} = 0,\ D_{s,p}\left.\frac{\partial c_p^s}{\partial r}\right\|_{r=R_p} = -j_p$ (10)

Since P2D requires a spatial system discrete (in x and r dimensions) via a finite difference method using a collection of differential equations in terms of the field variables, it usually will take minutes to hours to numerically solve the system depending on the solvers, routines, computers, etc [15]. For this work, the simulation of P2D is carried out in Dualfoil 5.0. Dualfoil is a FORTRAN program intended for the simulation of intercalation batteries developed by Paul Albertus and John Newman, in which the ten coupled nonlinear PDEs can be solved simultaneously by using the subroutine BAND with a finite difference method [16]. Note that the parameters used here in Table 3 are provided by the Dualfoil 5.0 program.

2.2. The single particle model

SP model incorporates the effects of transport phenomena in a simple manner. Zhang et al. [17] developed a model of diffusion and intercalation within a single electrode particle, which was expanded to a sandwich by considering the anode and cathode each as a single particle with the same surface area as the electrode [18]. In this model, diffusion and intercalation are considered within the particle, but the concentration and potential effects in the solution phase between the particles are neglected. Greater efficiency can be obtained by applying a volume average technique where a polynomial is used to approximate the concentration profile inside the particle. SP model is programmed and described with the following equations.

Firstly, SP model assumes that all of the particles in an electrode behave the same way and the current being passed through the electrode is distributed uniformly over all of the particles. Therefore, the pore wall flux of Li ions intercalate into or deintercalate from the particle is given as:

$$j_n = IR_n/3F\left(1-\varepsilon_n-\varepsilon_{f,n}\right)l_n \tag{23}$$

Table 2
Additional expressions of the P2D lithium-ion cell model [7].

Additional expressions	
$j_n = k_n\left(c^s_{\max,n} - c^s_n\big\vert_{r=R_n}\right)^{0.5} c^s_n\big\vert^{0.5}_{r=R_n} c^{0.5} 2\sinh\left(\frac{0.5F}{RT}\eta_n\right)$	(11)
$\eta_n = (\Phi_1 - \Phi_2 - U_n - R_{\mathrm{SEI},n} F j_n)$	(12)
$j_p = k_p\left(c^s_{\max,p} - c^s_p\big\vert_{r=R_p}\right)^{0.5} c^s_p\big\vert^{0.5}_{r=R_p} c^{0.5} 2\sinh\left(\frac{0.5F}{RT}\eta_p\right)$	(13)
$\eta_p = \left(\Phi_1 - \Phi_2 - U_p - R_{\mathrm{SEI},p} F j_p\right)$	(14)
$\kappa_{\mathrm{eff},i} = \varepsilon_i^{1.5}\left(0.0911 + 1.9101\times10^{-3}c - 1.052\times10^{-6}c^2 + 0.1554\times10^{-9}c^3\right),\ i = n,s,p$	(15)
$\sigma_{\mathrm{eff},i} = \sigma_i\left(1-\varepsilon_i-\varepsilon_{f,i}\right)^{1.5},\ i = n,p$	(16)
$D_{\mathrm{eff},i} = D\varepsilon_i^{1.5},\ i = n,s,p$	(17)
$a_i = \frac{3}{R_i}\left(1-\varepsilon_i-\varepsilon_{f,i}\right),\ i = n,p$	(18)
$U_n = 0.194 + 1.5\exp(-120\theta_n) + 0.0351\tanh[(\theta_n - 0.286)/0.083] - 0.0045\tanh[(\theta_n - 0.849)/0.119] - 0.035\tanh[(\theta_n - 0.9233)/0.05] - 0.0147\tanh[(\theta_n - 0.5)/0.034] - 0.102\tanh[(\theta_n - 0.194)/0.142] - 0.022\tanh[(\theta_n - 0.9)/0.0164] - 0.011\tanh[(\theta_n - 0.124)/0.0226] + 0.0155\tanh[(\theta_n - 0.105)/0.029]$	(19)
$\theta_n = \frac{c^s_n\big\vert_{r=R_n}}{c^s_{\max,n}}$	(20)
$U_p = 2.16216 + 0.07645\tanh(30.834 - 54.4806\theta_p) + 2.1581\tanh(52.294 - 50.294\theta_p) - 0.14169\tanh(11.0923 - 19.8543\theta_p) + 0.2051\tanh(1.4684 - 5.4888\theta_p) + 0.2531\tanh[(0.56478 - \theta_p)/0.1316] - 0.02167\tanh[(\theta_p - 0.525)/0.006]$	(21)
$\theta_p = \frac{c^s_p\big\vert_{r=R_p}}{c^s_{\max,p}}$	(22)

$$j_{\mathrm{p}} = -IR_{\mathrm{p}}/3F\left(1-\varepsilon_{\mathrm{p}}-\varepsilon_{\mathrm{f,p}}\right)l_{\mathrm{p}} \tag{24}$$

where I is the applied load current density on the electrode plates with the current being defined to be positive for discharging and negative for charging.

Secondly, considering the solid phase diffusion effect, the volume-averaged concentration of Li ions inside the particle and the concentration on the particle surface are given as:

$$c^s_{i,\mathrm{avg}} = c^s_{i,0} - \int_0^t 3\frac{j_i}{R_i}\mathrm{d}t,\ i = n,p \tag{25}$$

$$c^s_{i,\mathrm{surf}}(t) = c^s_{i,\mathrm{avg}}(t) + \left[8D_{s,i}q_{i,\mathrm{avg}}(t) - j_i\right]\cdot R_i/35D_{s,i} \tag{26}$$

where $q_{i,\mathrm{avg}}(t)$ is the volume-averaged concentration flux with zero initial value, which defines the average change of concentration with respect to the position in the system. For galvanostatic discharge, $q_{i,\mathrm{avg}}(t)$ has an analytical solution with an exponential form and the time constant are given as Eq. (27).

$$q_{i,\mathrm{avg}}(t) = \frac{3j_i}{4D_{s,i}}\left[\exp(-t/\tau_i^s) - 1\right],\ \tau_i^s = \frac{R_i^2}{30D_{s,i}},\ i = n,p \tag{27}$$

For the other operating conditions comprised of any type of charge–discharge operating scenarios, the recursive form should be used which is given by:

$$q_{i,\mathrm{avg}}(t_{k+1}) = q_{i,\mathrm{avg}}(t_k) - \left[\frac{45j_i}{2R_i^2} + 30\frac{D_{s,i}}{R_i^2}q_{i,\mathrm{avg}}(t_k)\right]\cdot(t_{k+1} - t_k) \tag{28}$$

The abovementioned Eqs. (26)–(28) are used to describe the solid phase diffusion process, which are on the basis of the solid phase diffusion governing equations, i.e. Eqs. (4) and (10), and deduced by applying a volume average technique where a

Table 3
Values of parameters used in the simulation.

Symbol	Description	Negative electrode	Separator	Positive electrode
$c^s_{\max,i}$	Maximum solid phase concentration (mol m^{-3})	24983		51218
$c^s_{i,0}$	Initial solid phase concentration (mol m^{-3})	19624		20046
c_0	Initial electrolyte concentration (mol m^{-3})	1000	1000	1000
D	Electrolyte diffusivity (m^2 s^{-1})	2.7877e-10	2.7877e-10	2.7877e-10
$D_{s,i}$	Solid Phase Diffusivity (m^2 s^{-1})	3.9e-14		1.0e-13
e	Faraday's Constant (C mol^{-1})		96487	
k_i	Reaction Rate constant (m$^{2.5}$ mol$^{-0.5}$ s^{-1})	1e-10		3e-11
l_i	Region thickness (m)	100e-6	25e-6	100e-6
R_i	Particle Radius (m)	10e-6		10e-6
$R_{SEI,i}$	SEI film resistance (Ωm^{-2})	5e-3		1e-3
R	Gas Constant (J mol^{-1} K^{-1})		8.314	
T	Temperature (K)		298	
t_+	Cationic transport number (−)		0.4	
$\varepsilon_{f,i}$	Filler fraction (−)	0.1		0.2
ε_i	Porosity (−)	0.3	1.0	0.3
σ_i	Solid phase conductivity (S m^{-1})	100		10
I	C rate times 1C discharge current density (A m^{-2})		C_rate × 30	

polynomial is used to approximate the concentration profile inside the particle.

The solid phase surface concentration of the particle determines the open circuit potential of the electrode. The difference in the open circuit potentials of the positive electrode and the negative electrode acts as the electromotive force (EMF) of the cell as a power supply. Therefore, the EMF is given as:

$$E = U_p\left(\frac{c^s_{p,\mathrm{surf}}}{c^s_{\max,p}}\right) - U_n\left(\frac{c^s_{n,\mathrm{surf}}}{c^s_{\max,n}}\right) \tag{29}$$

Thirdly, according to Butler–Volmer kinetics, the activation polarization overpotentials of the two electrodes are given as:

$$\eta_{\mathrm{act-polarization}} = \frac{2RT}{F}\left[\ln\left(\sqrt{m_n^2+1}+m_n\right) - \ln\left(\sqrt{m_p^2+1}+m_p\right)\right] \tag{30}$$

$$m_i = 0.5j_i \Big/ \left[k_i\left(c^s_{\max,i} - c^{s,}_{i,\mathrm{surf}}\right)^{0.5}\left(c^{s,}_{i,\mathrm{surf}}\right)^{0.5} c^{0.5}\right],\quad i = n,p \tag{31}$$

Additionally, the overpotential caused by the solid electrolyte interphase (SEI) film ohmic resistances are given as:

$$\eta_{\mathrm{SEI}} = R_{\mathrm{SEI},n}Fj_n - R_{\mathrm{SEI},p}Fj_p \tag{32}$$

Lastly, the EMF minus the two overpotentials is equal to the terminal voltage of the cell, which is given as:

$$V = E - \eta_{\mathrm{act-polarization}} - \eta_{\mathrm{SEI}} \tag{33}$$

With the assumption of the uniform reaction distribution, SP model considers each electrode as a single spherical particle. The solving procedure is to apply Eqs. (23)–(33) to solve $V(t)$ under load current $I(t)$ at different time step. Due to these simplifications, this model can be quickly simulated, but is only valid for limited conditions, such as low rates and thin electrodes [4]. For high rate operations, the accuracy of SP model degrades sharply with the increase of the charge–discharge rate. The essential reason is that, as the charge–discharge rate increases, the non-uniform reaction distribution effect is more and more serious, the concentration and potential distribution within the electrode and in the electrolyte cannot be neglected. Extending the description of the non-uniform reaction distribution effect is the key to solve the drawback of SP model at high C-rates.

3. The extended single particle model

This section mainly discusses how the ESP model is established, and it is organized as follows. In Section 3.1, the non-uniform

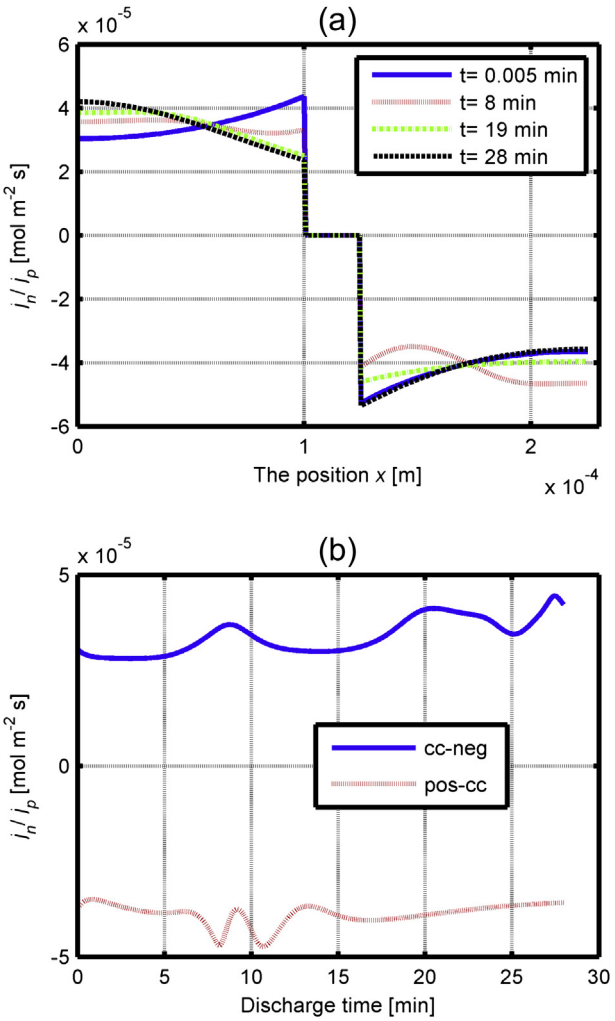

Fig. 2. (a) The pore wall flux j_n/j_p variations as a function of position x at different times under 2C rate discharge. (b) j_n/j_p at the two current collector interfaces varying with time.

reaction distribution effect inside the electrode and its mathematical description are analyzed in detail. In Section 3.2, an approximate solution of this effect is obtained by synthetically applying the volume average technique, approximated by the uniform reaction distribution situation, exponential profile approximation and the iterative calculation techniques. In Section 3.3, the expressions of the terminal voltage and the overpotentials are presented.

3.1. The non-uniform reaction distribution effect and the mathematical description

Without considering the self-heating phenomenon and the ambient thermal effect, describing the behavior of a cell is to evaluate the terminal voltage under the applied load current, i.e. $V = f(I)$. The essential of this issue is when the cell works in charge–discharge state, and when all the chemical and physical processes inside the cell take place simultaneously to provide current I for the outer electrical circuit, how much is the value of the difference in the potentials at the two current collector interfaces, i.e. the terminal voltage V.

Analyzing the relations of each limiting processes in the rigorous physics-based model, it can be concluded that the terminal voltage V is composed of four parts: the open circuit potential, the electrolyte phase potential, the activation polarization overpotential and the overpotential caused by the SEI film resistance. These four parts are all determined by the reactions at the two current collector interfaces. The degree of the local reactions can be represented with the pore wall fluxes at the two current collector interfaces ($x = 0$ and $x = l_{tot} = l_n + l_s + l_p$), i.e. $j_n(0, t)/j_p(l_{tot}, t)$.

The behavior of the battery with parameters in Table 3 is simulated with P2D model. The result of the non-uniform reaction distribution effect is illustrated in Fig. 2. Fig. 2a illustrates j_n/j_p variations as a function of position x at different times under 2C rate discharge, and Fig. 2b illustrates that the pore wall fluxes at the two current collector interfaces vary with time. The interface between the current collector and the negative electrode is marked as cc-neg, and the interface between the positive electrode and the current collector is marked as pos-cc, respectively.

It can be seen that, when the battery works in charge/discharge state, the reaction currents at different positions along x-axis are non-uniform, and the distributions change with time. The pore wall fluxes at the two current collector interfaces under galvanostatic discharge do not maintain a constant value, but changes over time. How to obtain the pore wall fluxes $j_n(0, t)/j_p(l_{tot}, t)$ at the two current collector interfaces under applied current I is the key to describe the non-uniform reaction distribution effect, and it is also the key to correctly calculating the terminal voltage V.

Analyzing the original physics-based P2D model, the reaction distribution along x-axis is the combined effects of the solid/electrolyte phase ohmic effects, the concentration polarization in the electrolyte, the difference of the open circuit potentials resulted from different solid-phase surface ion concentrations, and the SEI film resistance ohmic effects at different positions. The essential issue is to analyze the reaction difficulty at different positions along x-axis.

The mathematical description of the non-uniform reaction distribution effect is explained taking the negative electrode for example. In the original physics-based model, Eq. (12) describes the potential balance inside the electrode. In other words, the potentials within the electrode satisfy the following equation at any position and any time.

$$\eta_n(x,t) = \left(\Phi_1(x,t) - \Phi_2(x,t) - U_n(x,t) - R_{SEI,n}Fj_n(x,t)\right) \tag{34}$$

Taking the derivation of each variable in the above equation with respect to x, we obtain that the distributions of the potentials along x-axis and the pore wall flux distribution satisfy the following relation:

$$\frac{\partial\eta_n(x,t)}{\partial x} = \frac{\partial\Phi_1(x,t)}{\partial x} - \frac{\partial\Phi_2(x,t)}{\partial x} - \frac{\partial U_n(x,t)}{\partial x} - R_{SEI,n}F\frac{\partial j_n(x,t)}{\partial x} \tag{35}$$

The above Eq. (35) is just the mathematical description of the non-uniform reaction distribution effect for the negative electrode. It is the key to obtaining the pore wall flux $j_n(x,t)$ which satisfies Eq. (35).

3.2. An approximate solution of the non-uniform reaction distribution effect

3.2.1. Obtaining the approximate solution of the relation between the activation polarization overpotential distribution and the pore wall flux distribution based on volume average technique

In P2D model, the relation between the activation polarization overpotential $\eta_n(x,t)$ and the pore wall flux $j_n(x,t)$ is described as Eq. (11), which is given as:

$$j_n(x,t) = k_n\left(c^s_{max,n} - c^s_n(x,t)\big|_{r=R_n}\right)^{0.5} c^s_n(x,t)\big|^{0.5}_{r=R_n} c(x,t)^{0.5} 2\sinh\left(\frac{0.5F}{RT}\eta_n(x,t)\right)$$

It can be seen that, the relation of these two variables is affected by the solid phase and electrolyte phase local ion concentrations at different positions. In order to obtain an approximate solution, the volume average technique is used here. The local concentrations at different positions are approximated with the average concentration value within the whole electrode volume. Therefore, the electrolyte phase local ion concentrations are approximated as $c(x,t) \approx c_0$. The solid phase ion concentrations are approximated and calculated as follow:

$$c^s_n(x,t) \approx c^s_n(t) = c^s_{n,0} - \frac{I}{F\left(1 - \varepsilon_n - \varepsilon_{f,n}\right)l_n}\cdot t \tag{36}$$

Then, the relation between the activation polarization overpotential distribution and the pore wall flux distribution can be described as:

$$\frac{\partial\eta_n(x,t)}{\partial x} \approx \frac{d\eta}{dj}(t)\cdot\frac{\partial j_n(x,t)}{\partial x} \tag{37}$$

where

$$\frac{d\eta}{dj}(t)=\frac{RT}{F}\cdot\frac{1}{\sqrt{m_n^2+1}}\cdot\frac{1}{k_n\left(c^s_{\max,n}-c^s_n(t)\right)^{0.5}c^s_n(t)^{0.5}c_0^{0.5}}$$
$$m_n=\frac{1}{2}\cdot\frac{1}{k_n\left(c^s_{\max,n}-c^s_n(t)\right)^{0.5}c^s_n(t)^{0.5}c_0^{0.5}}\cdot\frac{I\cdot R_n}{3F\left(1-\varepsilon_n-\varepsilon_{f,n}\right)l_n} \quad (38)$$
$$c^s_n(t)=c^s_{n,0}-\frac{I}{F\left(1-\varepsilon_n-\varepsilon_{f,n}\right)l_n}\cdot t$$

3.2.2. The approximate solution of the solid phase potential distribution and electrolyte phase potential distribution approximated by the uniform reaction distribution situation

The distributions of the solid phase potential and the electrolyte phase potential inside the electrode are determined by three effects: the solid phase ohmic effect, the electrolyte phase ohmic effect and the electrolyte concentration polarization effect. Generally, the electrode material and the electrolyte have a good conductivity in order to improve the battery performance. Therefore, the solid phase and electrolyte phase ohmic effects have less influence than other governing processes. Therefore, in this work, the solid phase potential distribution and electrolyte phase potential distribution are approximated by the uniform reaction distribution situation. As for the potential distribution caused by the electrolyte concentration polarization effect, its approximate solution is obtained based on the approximate analytical solution for the electrolyte concentration distribution proposed by the authors in previous research article [11]. The detailed results are listed as follow:

The solid phase potential distribution $\partial\Phi_1(x,t)/\partial x$ is approximated by the uniform reaction distribution situation, which is given as:

$$\frac{\partial\Phi_1(x,t)}{\partial x}\approx-\frac{I}{\sigma_{\mathrm{eff},n}\cdot l_n}(l_n-x) \quad (39)$$

The electrolyte phase potential distribution $\partial\Phi_2(x,t)/\partial x$ is approximated as:

$$\frac{\partial\Phi_2(x,t)}{\partial x}\approx-\frac{I}{\kappa_{\mathrm{eff},n}\cdot l_n}\cdot x-\frac{2RT}{F}\cdot(1-t_+)\cdot\frac{-(P_1x)\cdot(1-\exp(-t/\tau_n))\cdot I}{\left(\frac{1}{2}P_1x^2+P_2\right)\cdot(1-\exp(-t/\tau_n))\cdot I+c_0} \quad (40)$$

In the above Eq. (40), the first item represents the electrolyte phase ohmic effect which is approximated by the uniform reaction distribution situation, and the second item represents the electrolyte concentration polarization effect which is obtained based on the approximate analytical solution for the electrolyte concentration distribution proposed by the authors before [11]. In the second item, P_1, P_2, τ_n are constants, which are calculated as follow:

$$P_1=\frac{(1-t_+)}{D\cdot F}\cdot\frac{-1}{\varepsilon_n^{1.5}\cdot l_n} \quad (41)$$

$$P_2=\frac{(1-t_+)}{D\cdot F}\cdot\left[\frac{1}{\varepsilon_n l_n+\varepsilon_s l_s+\varepsilon_p l_p}\cdot\left(\frac{1}{6}\cdot\frac{l_n^2}{\varepsilon_n^{0.5}}+\frac{1}{2}\cdot\frac{l_s^2}{\varepsilon_s^{0.5}}+\frac{1}{3}\cdot\frac{l_p^2}{\varepsilon_p^{0.5}}+\frac{1}{2}\cdot\frac{\varepsilon_s l_n l_s}{\varepsilon_n^{1.5}}+\frac{\varepsilon_p l_s l_p}{\varepsilon_s^{1.5}}+\frac{1}{2}\cdot\frac{\varepsilon_p l_n l_p}{\varepsilon_n^{1.5}}\right)\right] \quad (42)$$

$$\tau_n=\frac{-1}{D\varepsilon_n^{0.5}}\cdot\frac{P_2}{P_1} \quad (43)$$

3.2.3. The solution of the open circuit potential distribution based on exponential profile approximation

The open circuit potential distribution $\partial U_n(x,t)/\partial x$ is an important factor which determines the reaction distribution within the electrode. It is resulted from different solid-phase surface ion concentrations at different positions along x-axis, and different electrode materials have their own open circuit potential profiles with different forms. Therefore, there is not a uniform mathematical expression to describe the open circuit potential distribution. In order to approximately calculate the influence of this effect and to improve the computational efficiency, this work considers to describe this effect with certain analytic function. The results show that, the exponential function can be used to describe the open circuit potential distribution with good accuracy. Then the open circuit potential is assumed to be an exponential profile along x-axis, which is given as:

$$U_n(x,t)\approx a(t)\cdot\exp(b(t)\cdot x)+d(t) \quad (44)$$

where $a(t)/b(t)/d(t)$ are three time-varying coefficients. The distribution of the open circuit potential is given as:

$$\frac{\partial U_n(x,t)}{\partial x}\approx a(t)\cdot b(t)\cdot\exp(b(t)\cdot x) \quad (45)$$

Based on the above approximations, i.e. Eqs. (37)–(45), the issue of the non-uniform reaction distribution effect described in Eq. (35) can be re-described as:

$$\left(\frac{d\eta}{dj}(t)+R_{\mathrm{SEI},n}F\right)\cdot\frac{\partial j_n(x,t)}{\partial x}=\frac{2RT}{F}\cdot(1-t_+)\cdot\frac{-(P_1x)\cdot(1-\exp(-t/\tau_n))\cdot I}{\left(\frac{1}{2}P_1x^2+P_2\right)\cdot(1-\exp(-t/\tau_n))\cdot I+c_0}+\frac{I}{l_n}\left(\frac{1}{\sigma_{\mathrm{eff},n}}+\frac{1}{\kappa_{\mathrm{eff},n}}\right)\cdot x-a(t)\cdot b(t)\cdot\exp(b(t)\cdot x)-\frac{I}{\sigma_{\mathrm{eff},n}} \quad (46)$$

Eq. (46) has an analytical solution of $j_n(x,t)$, it is given as:

$$j_n(x,t) = \mathrm{const}(t) + \frac{1}{\left(\frac{d\eta}{dj}(t) + R_{\mathrm{SEI},n}F\right)} \cdot \left\{ \begin{array}{l} \frac{2RT}{F}\cdot(1-t_+)\cdot\ln\left(\frac{P_2\cdot(1-\exp(-t/\tau_n)\cdot I + c_0}{\left(\frac{1}{2}P_1x^2+P_2\right)\cdot(1-\exp(-t/\tau_n))\cdot I + c_0}\right) \\ +\frac{I}{l_n}\left(\frac{1}{\sigma_{\mathrm{eff},n}}+\frac{1}{\kappa_{\mathrm{eff},n}}\right)\cdot\frac{x^2}{2} - a(t)\cdot\exp(b(t)\cdot x) - \left(\frac{I}{\sigma_{\mathrm{eff},n}}\right)\cdot x \end{array} \right\} \quad (47)$$

where the constant const(t) is solvable according to another condition: the integration of the pore wall fluxes at different positions within the whole electrode is a determined value. This determined value is proportional to the applied load current. This condition is described as:

$$\int_0^{l_n} j_n(x,t)\mathrm{d}x = \frac{I\cdot R_n}{3F\left(1-\varepsilon_n-\varepsilon_{f,n}\right)}$$

Then, the constant $const(t)$ is solved and the result is:

$$\mathrm{const}(t) = \frac{I\cdot R_n}{3F\left(1-\varepsilon_n-\varepsilon_{f,n}\right)\cdot l_n} - \frac{1}{\left(\frac{d\eta}{dj}(t)+R_{\mathrm{SEI},n}F\right)\cdot l_n}\cdot e(t)$$

$$e(t) = \left\{ \begin{array}{l} \frac{2RT}{F}\cdot(1-t_+)\cdot\left(l_n\cdot\ln\left(\frac{g(t)}{-z(t)l_n^2+g(t)}\right)+2l_n-2\sqrt{\frac{g(t)}{z(t)}}\cdot\mathrm{arctanh}\left(\sqrt{\frac{z(t)}{g(t)}}\cdot l_n\right)\right) \\ +I\cdot\left(\frac{1}{\sigma_{\mathrm{eff},n}}+\frac{1}{\kappa_{\mathrm{eff},n}}\right)\cdot\frac{l_n^2}{6} - \frac{a(t)}{b(t)}\cdot(\exp(b(t)\cdot l_n)-1) - \left(\frac{I}{\sigma_{\mathrm{eff},n}}\right)\cdot\frac{l_n^2}{2} \end{array} \right\} \quad (48)$$

$$z(t) = -\left(\frac{1}{2}P_1\cdot(1-\exp(-t/\tau_n))\cdot I\right)$$

$$g(t) = (P_2\cdot(1-\exp(-t/\tau_n))\cdot I + c_0)$$

Summing up the above analysis in Section 3.2, after the simplification based on the volume average technique, the exponential profile approximation, and approximation by the uniform reaction distribution situation, the analytical solution of $j_n(x,t)$ is obtained, i.e. Eq. (47). In addition, the solving method of the time-varying coefficients $a(t)/b(t)/d(t)$ in the exponential profile of the open circuit potential should be considered. It is explained in the next section.

3.2.4. Solving the time-varying coefficients a(t)/b(t)/d(t) by iterative calculation

At the initial time step $t = 0$, the solid-phase surface ion concentrations at different positions along x-axis are equal, and the open circuit potentials at different positions are also equal. Therefore, at the initial time step, the coefficients $a(0) = 0$, $b(0)$ can be an arbitrary value. According to Eqs. (47) and (48), the pore wall flux distribution at the initial time step can be solved, it is given as:

$$j_n(x,0) = \mathrm{const}(0) + \frac{1}{\left(\frac{d\eta}{dj}(0)+R_{\mathrm{SEI},n}F\right)}\cdot\left[\frac{I}{l_n}\left(\frac{1}{\sigma_{\mathrm{eff},n}}+\frac{1}{\kappa_{\mathrm{eff},n}}\right)\cdot\frac{x^2}{2} - \left(\frac{I}{\sigma_{\mathrm{eff},n}}\right)\cdot x\right] \quad (49)$$

Three typical active particles within the electrode are selected evenly, which three points are $x = 0$, $x = 0.5l_n$ and $x = l_n$ and which are illustrated in Fig. 3.

At the initial time step $t = 0$, the pore wall fluxes of the three selected particles are $j_n(0,0)$, $j_n(0.5l_n,0)$ and $j_n(l_n,0)$ respectively. Then, the single particle computation subroutine is applied to the three particles, respectively.

The single particle computation subroutine is a calculation process which calculates the behavior of the single particle under a certain pore wall flux, and it outputs the open circuit potential at the next time step under current pore wall flux, i.e. $j_n(x,t_k)\rightarrow U_n(x,t_{k+1})$. This single particle computation subroutine is

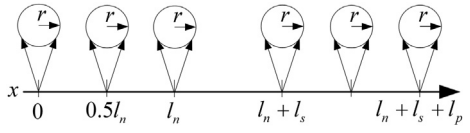

Fig. 3. The three selected particles in the iterative calculation.

illustrated in Fig. 4, and it is composed of three steps. Step 1 calculates the solid-phase average ion concentration of the particle at the next time step under current pore wall flux, using the following equation:

$$c^s_{n,\mathrm{avg}}(x,t_{k+1}) = c^s_{n,\mathrm{avg}}(x,t_k) - 3\frac{j_n(x,t_k)}{R_n}\cdot(t_{k+1}-t_k) \tag{50}$$

Step 2 calculates the solid-phase surface ion concentration under the effect of solid-phase diffusion inside the particle. This calculation is with the same method in SP model, using Eqs. (26)–(28).

Step 3 calculates the open circuit potential, using the expression $U_n(c^s_{n,\mathrm{surf}}(x,t_{k+1})/c^s_{\mathrm{max},n})$.

Thus, the open circuit potentials of the three selected particles at time step t_1 can be obtained, which are $U_n(0,t_1)$, $U_n(0.5l_n,t_1)$ and $U_n(l_n,t_1)$.

As for the other time steps $t = t_k(k \geq 1)$, the coefficients $a(t)$/$b(t)$/$d(t)$ are calculated as follow.

The open circuit potential profile is an exponential function along x-axis, i.e. $U_n(x,t_k) = a(t_k)\cdot\exp(b(t_k)\cdot x) + d(t_k)$, and the potentials at the three selected particle points are known, i.e. $U_n(0,t_k)$/$U_n(0.5l_n,t_k)$/$U_n(l_n,t_k)$. Therefore, the coefficients $a(t_k)$/$b(t_k)$/$d(t_k)$ can be calculated with the following equation:

$$\begin{aligned} d(t_k) &= \frac{U_n(0.5l_n,t_k)^2 - U_n(0,t_k)\cdot U_n(l_n,t_k)}{2U_n(0.5l_n,t_k) - U_n(0,t_k) - U_n(l_n,t_k)} \\ b(t_k) &= \frac{\ln\left(\dfrac{U_n(0,t_k)-d(t_k)}{U_n(0.5l_n,t_k)-d(t_k)}\right)}{-0.5l_n} \\ a(t_k) &= U_n(0,t_k) - d(t_k) \end{aligned} \tag{51}$$

Then, the pore wall flux distribution at time step t_k, i.e. $j_n(x,t_k)$ is solved according to Eqs. (47) and (48). The open circuit potentials of the three selected particles at the next time step, i.e. $U_n(0,t_{k+1})$\$U_n(0.5l_n,t_{k+1})$\$U_n(l_n,t_{k+1})$ are calculated using the single particle computation subroutine. Then the coefficients at the next time step $a(t_{k+1})$/$b(t_{k+1})$ are calculated with Eq. (51), and the pore wall flux distribution at the next time step $j_n(x,t_{k+1})$ is calculated. Thus, the iterative calculation from current time step to the next time step is realized.

3.2.5. Summary of this section

An approximate solution of the non-uniform reaction distribution effect is obtained in this section. The simplified methods used here include the volume average technique, approximated by the uniform reaction distribution situation, the exponential profile approximation and the iterative calculation. The solving procedure of the pore wall flux distribution is summarized and illustrated in Fig. 5.

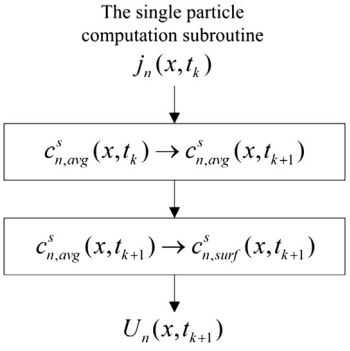

Fig. 4. Illustration of the single particle computation subroutine.

3.3. Computation of the terminal voltage

Based on the approximate solution of the non-uniform reaction distribution effect in Section 3.2, the pore wall fluxes at the two current collector interfaces $j_n(0,t)$/$j_p(l_{\mathrm{tot}},t)$ can be calculated. Then, the behavior of the two particles at the two current collector interfaces can be calculated with the same method in SP model. The solid-phase average ion concentration $c^s_{i,\mathrm{avg}}$ and the surface ion concentration $c^s_{i,\mathrm{surf}}$ of the particle are calculated with Eqs. (25)–(28). The electromotive force E is calculated with Eq. (29). The activation polarization overpotential $\eta_{\mathrm{act-polarization}}$ is calculated with Eqs. (30)–(31), and the SEI film resistance overpotential η_{SEI} is calculated with Eq. (32). It is worthy to note that, as differentiated from SP model, ESP model firstly solves the pore wall flux distribution and then calculates the behavior of the two particles at the current collector interfaces. Therefore, ESP model extends the description of the non-uniform reaction distribution effect. Additionally, ESP model also extends the calculation of the overpotential caused by the concentration polarization in the electrolyte and the ohmic effects. This overpotential is defined as the electrolyte overpotential $\eta_{\mathrm{electrolyte}}$. Lastly, the terminal voltage in ESP model is equal to the EMF minus the three overpotentials, which is given as:

$$V = E - \eta_{\mathrm{act-polarization}} - \eta_{\mathrm{SEI}} - \eta_{\mathrm{electrolyte}} \tag{52}$$

where the electrolyte overpotential $\eta_{\mathrm{electrolyte}}$ represents the difference in the electrolyte-phase potentials at the two current collector interfaces. It describes the overpotentials caused by the diffusion in the electrolyte and the ohmic effects, and it consists of three parts: the electrolyte concentration polarization overpotential, the electrolyte-phase ohmic overpotential, and the solid-phase ohmic overpotential. Based on the approximate analytical solution for the electrolyte concentration distribution proposed by the authors before [11], the calculation equations of $\eta_{\mathrm{electrolyte}}$ are given as follow:

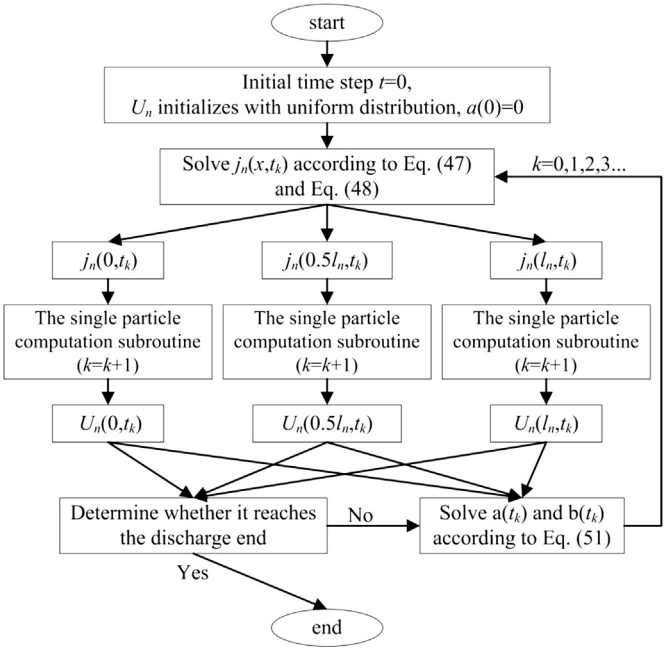

Fig. 5. Illustration of the pore wall flux distribution solving procedure.

$$\eta_{\text{electrolyte}} = \Phi_2\big|_{x=0} - \Phi_2\big|_{x=l_{\text{tot}}} = \left(\eta_{\text{con-polarization}} + \eta_{\text{liquid-ohm}} + \eta_{\text{solid-ohm}}\right) \tag{53}$$

where the electrolyte concentration polarization overpotential is given as:

$$\eta_{\text{con-polarization}} = 2\frac{RT}{F}(1-t_+)\cdot\left(\ln c_n^{cc} - \ln c_p^{cc}\right) \tag{54}$$

where c_n^{cc} is the electrolyte concentration at the negative current collector interface, which is given as:

$$c_n^{cc} = c(0,t) = P_2\cdot\left(1-e^{-t/\tau_n}\right)\cdot i_{\text{app}} + c_0 \tag{55}$$

c_p^{cc} is the electrolyte concentration at the positive current collector interface, which is given as:

$$c_p^{cc} = c(l_{\text{tot}},t) = P_6\cdot\left(1-e^{-t/\tau_p}\right)\cdot i_{\text{app}} + c_0 \tag{56}$$

where $P_2/\tau_n/P_6/\tau_p$ are computable constants, and their detailed definitions are in the reference article [11]. The electrolyte phase ohmic overpotential and the solid-phase ohmic overpotential are also approximated by the uniform reaction distribution situation, which are given as:

$$\eta_{\text{liquid-ohm}} \approx \left(\frac{0.5l_n}{\kappa_{\text{eff},n}} + \frac{l_s}{\kappa_{\text{eff},s}} + \frac{0.5l_p}{\kappa_{\text{eff},p}}\right)\cdot I \tag{57}$$

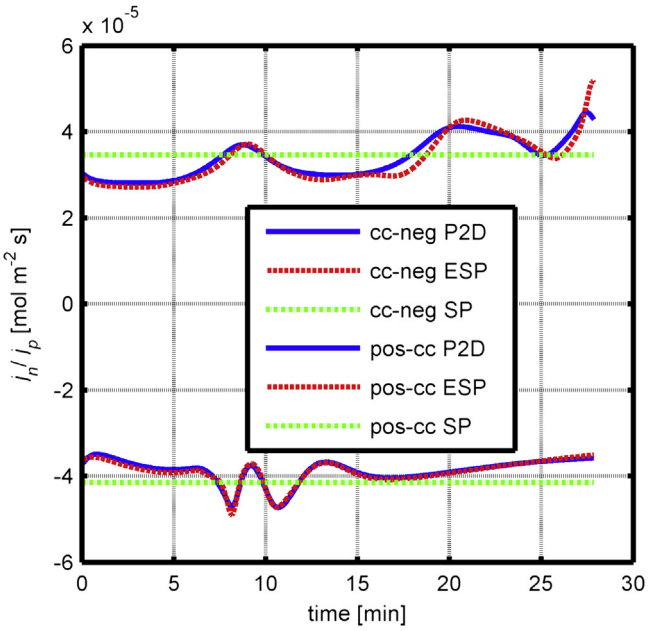

Fig. 7. Comparison of the pore wall fluxes at the two current collector interfaces simulated by SP ESP and P2D models under 2C rate discharge.

$$\eta_{\text{solid-ohm}} \approx \frac{1}{2}\cdot\left(\frac{l_n}{\sigma_{\text{eff},n}} + \frac{l_p}{\sigma_{\text{eff},p}}\right)\cdot I \tag{58}$$

Summarizing all the descriptions in Section 3, ESP model is established. This model has two main extensions. One is the

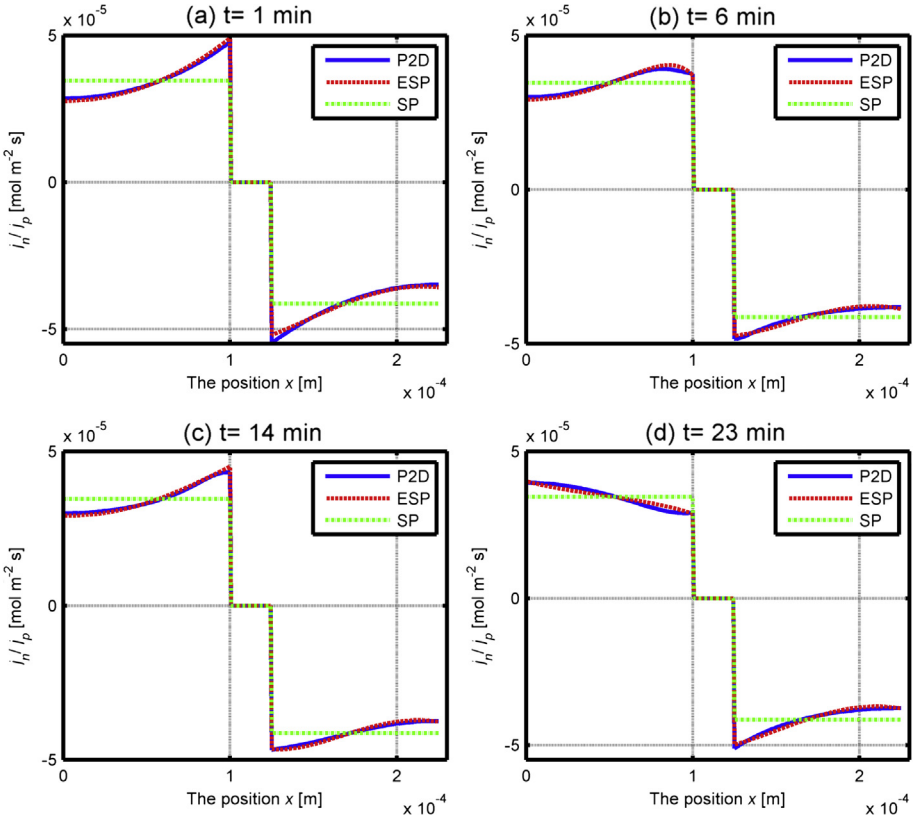

Fig. 6. Comparison of the pore wall flux distributions along x-axis simulated by SP ESP and P2D models at t = 1/6/14/23 min under 2C rate discharge.

approximate solution of the non-uniform reaction distribution effect, which makes the pore wall fluxes at the two current collector interfaces under different charge–discharge conditions solvable. The other is the electrolyte overpotential caused by the concentration polarization in the electrolyte and the ohmic effects.

Summarizing the equations of ESP model include: Eqs. (47),(48), Eq. (50), Eqs. (26)–(28), Eq. (19), Eq. (51), Eqs. (25)–(32), Eq. (52), and Eqs. (53)–(58). The solving procedure of the pore wall flux distribution and the single particle computation subroutine are illustrated as Figs. 4 and 5, respectively.

4. Results and discussion

The validation of ESP model and its comparison with SP and P2D models are discussed in this section. For this work, the simulation of P2D is carried out in Dualfoil 5.0 program compiled with the FORTRAN compiler g77. In Dualfoil, the ten coupled nonlinear PDEs are solved simultaneously by using the subroutine BAND with a finite difference method. The result simulated in Dualfoil is considered as the exact solution and is used to compare with the result from ESP model. For SP and ESP model, their equations and solving procedures are programmed and simulated in MATLAB R2009b software. All the simulations are carried out on a PC with Intel Core i3 CPU 530 @ 2.93 GHz, 2.99 GB RAM and Windows operating system.

4.1. 2C galvanostatic discharge

Under 2C galvanostatic discharge, the pore wall flux distribution along x-axis is simulated with ESP and P2D models. The result

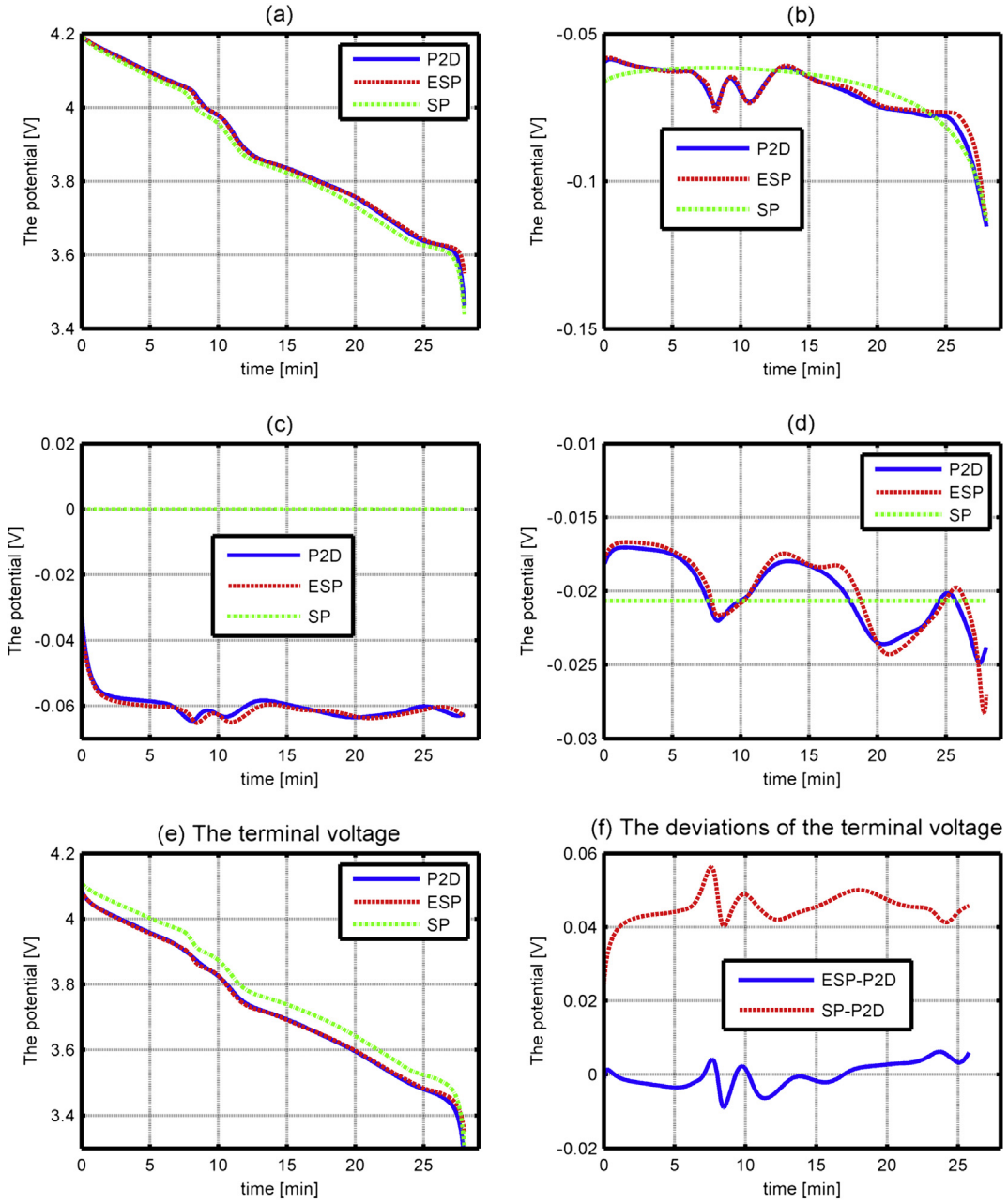

Fig. 8. Comparison of (a) the electromotive force (b) the activation polarization overpotential (c) the electrolyte overpotential (d) the SEI film resistance overpotential and (e) the terminal voltage simulated by SP ESP and P2D models under 2C rate discharge. Figure (f) illustrates the deviations of the terminal voltage profiles.

fluxes at four different discharge time $t = 1/6/14/23$ min are presented in Fig. 6. At the same time, the fluxes used in SP model are also plotted in the figure for comparison.

The following results can be seen from Fig. 6. SP model assuming that the reactions inside the electrode are with a uniform distribution and the pore wall fluxes at different positions maintain a constant value, but the exact results simulated by P2D model show that the pore wall fluxes at different positions along x-axis are non-uniform and the distributions change with time. ESP model extends the description of the non-uniform reaction distribution effect, and therefore it can approximately simulate the pore wall flux distributions at different times. The result flux distributions simulated by ESP model agree well with the results from P2D model.

The key to calculating the non-uniform reaction distribution effect is to obtain the pore wall fluxes $j_n(0, t)$ and $j_p(l_{tot}, t)$ at the two current collector interfaces accurately. The results simulated by SP ESP and P2D model are plotted and compared in Fig. 7.

From Fig. 7, similarly it can be seen that, SP model considers the pore wall fluxes at the two current collector interfaces maintaining a constant value under galvanostatic discharge. ESP model can accurately predict the reactions at the current collector interfaces under the influence of the non-uniform reaction distribution effect. The flux profiles simulated by ESP model agree well with the results from P2D model under 2C rate discharge.

Based on a more accurate prediction of the reactions at the two interfaces, the EMF and the three overpotentials and the terminal voltage simulated by ESP model also improve compared with SP model. Their comparison under 2C rate discharge is illustrated in Fig. 8.

From Fig. 8, it can be seen that the results simulated by ESP model improve significantly compared with SP model. In Fig. 8a,

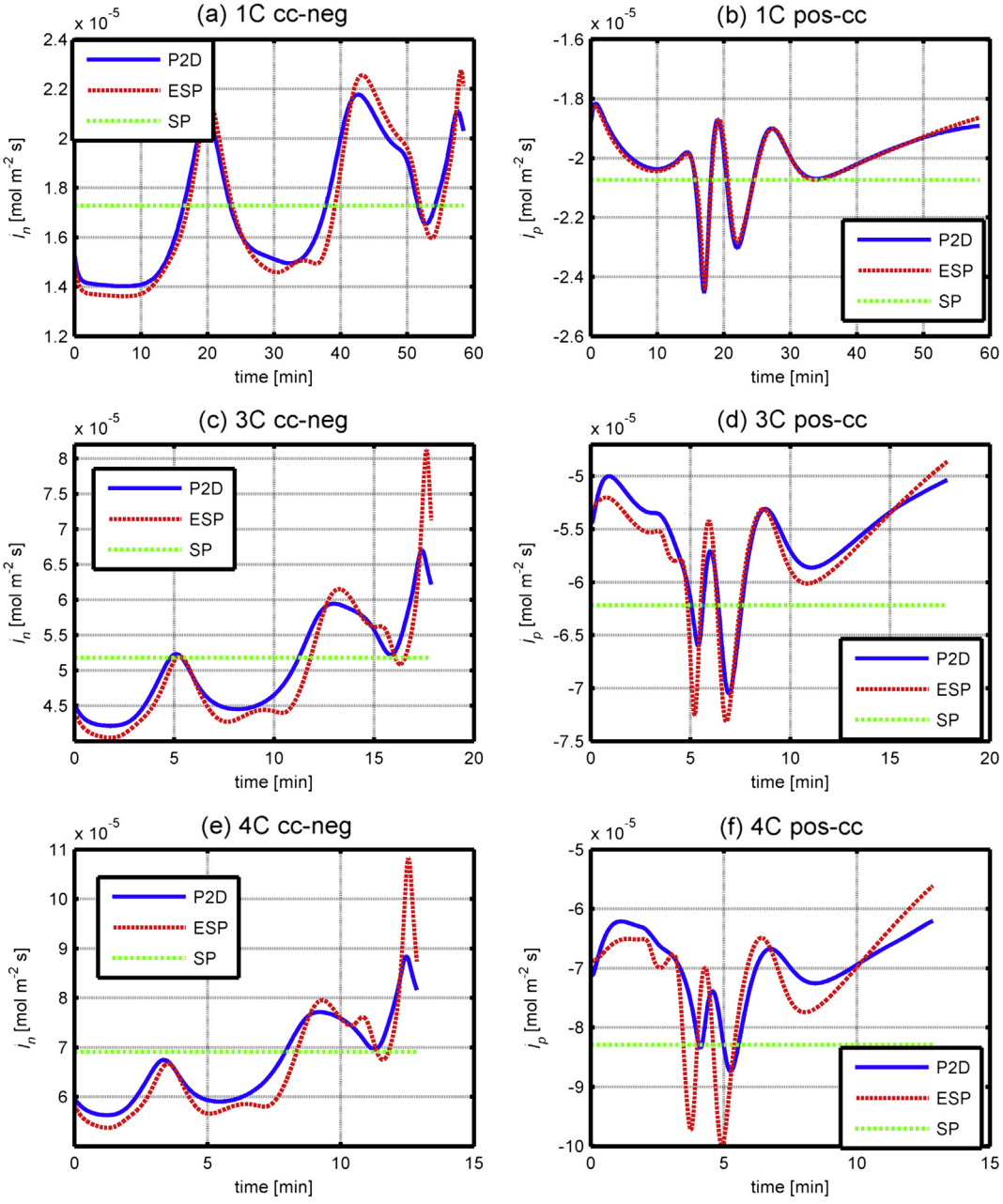

Fig. 9. Comparison of the pore wall fluxes at the cc-neg interface and the pos-cc interface simulated by SP ESP and P2D models under 1C/3C/4C rate discharges.

the EMF simulated by ESP model is more accurate than SP model compared with the exact solution from P2D model. Especially for the electrolyte overpotential in Fig. 8c, SP model assumes this overpotential is zero, but ESP model can calculate this overpotential and the result profile agrees well with the electrolyte overpotential from P2D model. As for the activation polarization overpotential in Fig. 8b and the SEI film resistance overpotential in Fig. 8d, SP model can only estimate an average value, but ESP model can simulate the detail fluctuations in the overpotential profiles. With a more accurate EMF and the three overpotentials, the terminal voltage simulated by ESP model also improves as illustrated in Fig. 8e. Fig. 8f illustrates the deviations of the terminal voltage profiles simulated by SP/ESP model with respect to P2D model, which are marked as SP-P2D and ESP-P2D respectively. It can be seen that the maximum error of the terminal voltage values from SP model is 56.2 mV, and that of ESP model is only 8.9 mV under 2C rate discharge. All the improvements are attributed to the approximate solution of the non-uniform reaction distribution effect. This extension makes it possible for the pore wall fluxes at the two current collector interfaces to be accurately calculated.

4.2. Galvanostatic discharges with different C-rates

1C 3C and 4C rate discharges are selected to study the performance of ESP model under different C-rates. Firstly, the pore wall fluxes at the two current collector interfaces under 1C/3C/4C rate discharges are plotted in Fig. 9.

From Fig. 9 it can be seen that, under different C-rate discharges, ESP model can approximately predict the reactions at the two current collector interfaces. The pore wall flux values under different C-rates calculated by ESP model are correct, and the fluctuations in the flux profiles during the discharge are also

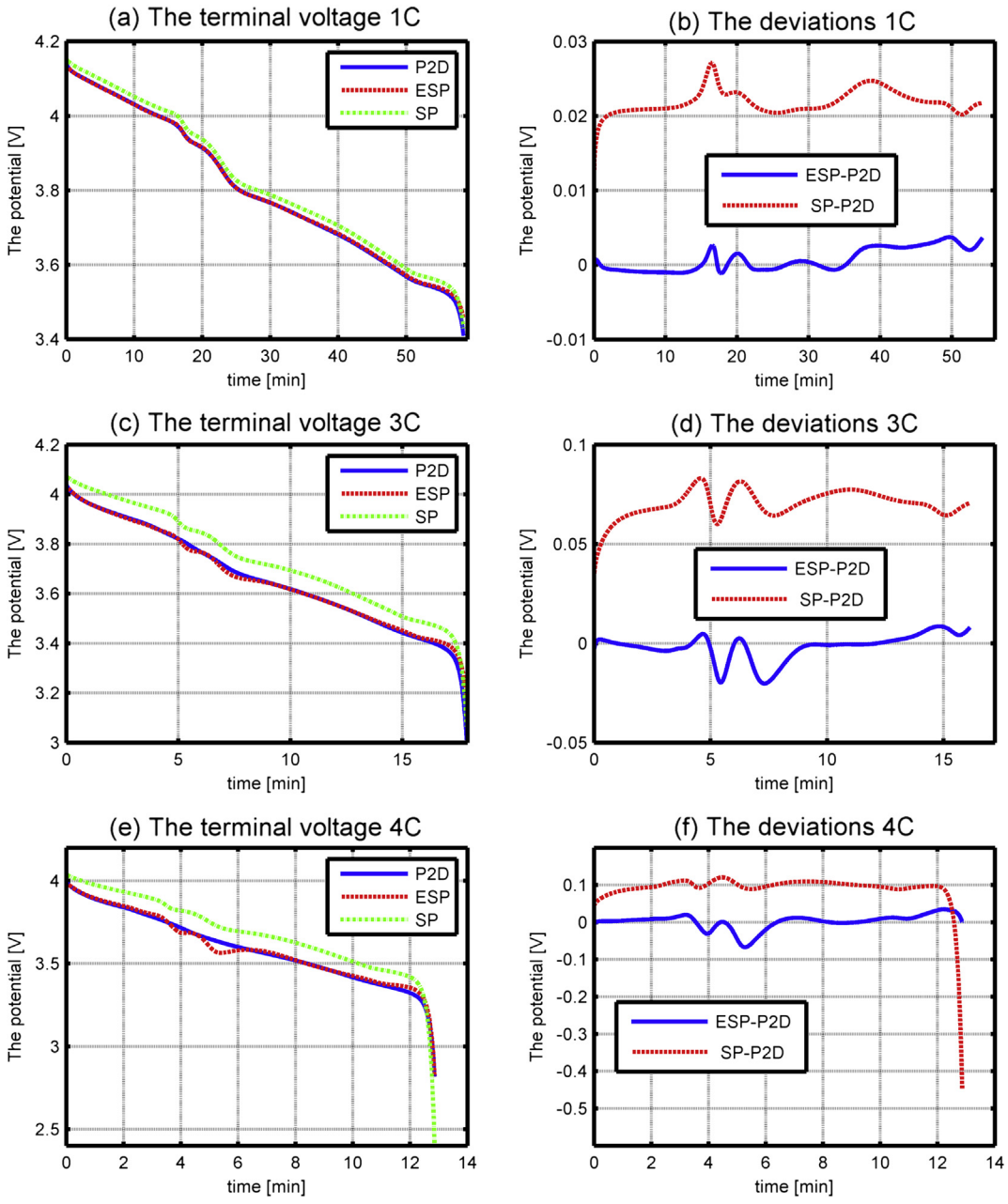

Fig. 10. Comparison of the terminal voltage profiles simulated by SP ESP and P2D models under 1C/3C/4C rate discharges.

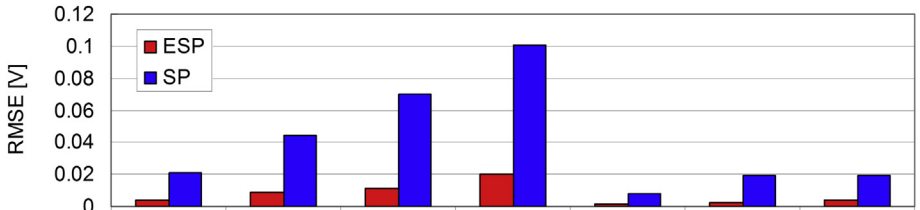

	1C discharge	2C discharge	3C discharge	4c discharge	0.5C CCCV	4C DST discharge	4C FUDS discharge
ESP	0.0044	0.0087	0.0114	0.0199	0.0015	0.0024	0.0039
SP	0.0207	0.044	0.0699	0.1009	0.0081	0.0197	0.0192

Fig. 11. The RMSEs between the terminal voltage profiles predicted by ESP/SP model and those from P2D model under different operating conditions.

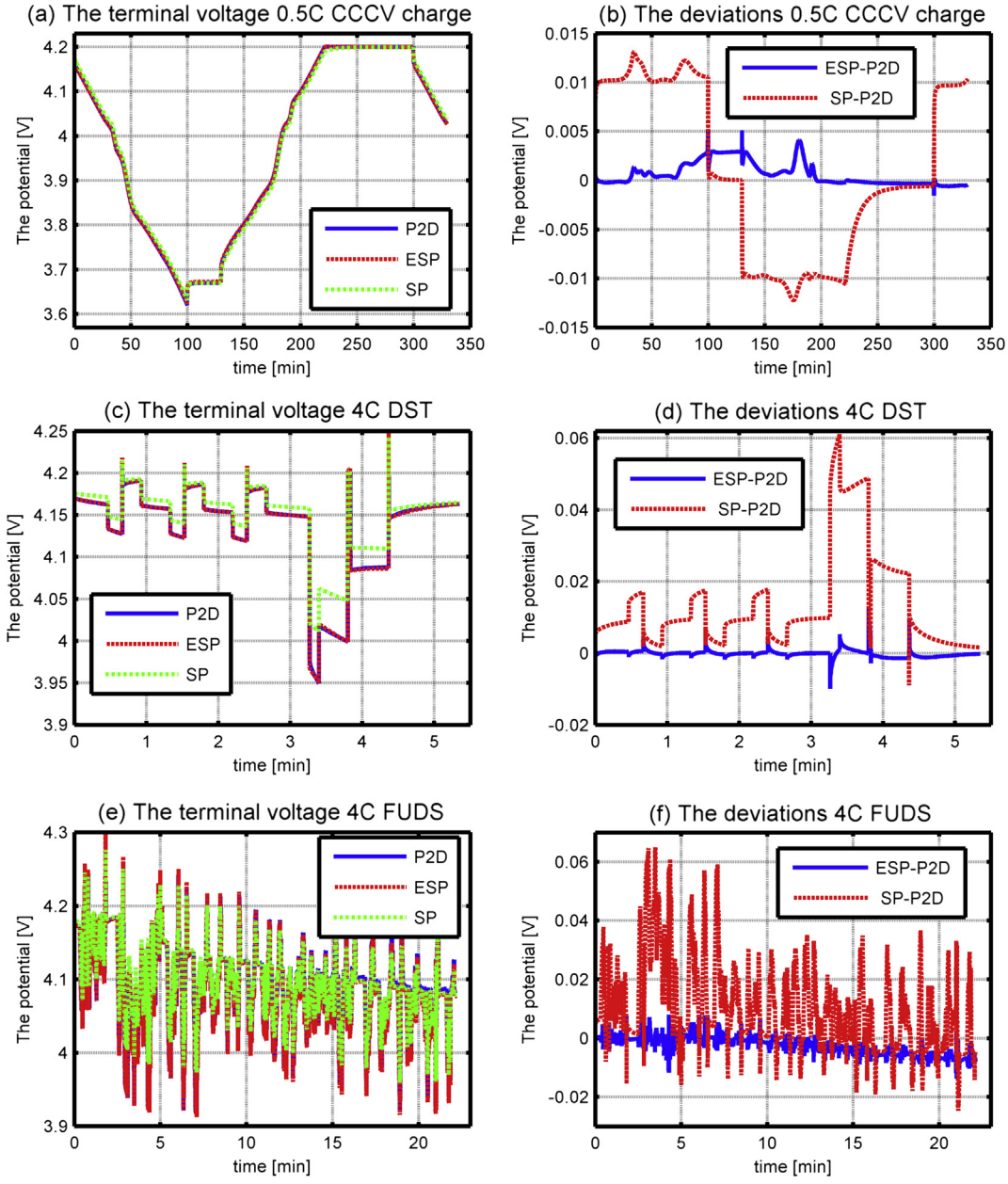

Fig. 12. Comparison of the terminal voltage profiles simulated by SP ESP and P2D models under 0.5C CCCV charge, DST and FUDS discharges.

simulated approximately with a small error. Also it can be seen that the deviation between the fluxes from ESP model and that from P2D model increases with the increase of the discharge C-rates. Especially for the fluxes at the pos-cc interface in Fig. 9f under 4C rate discharge, the result profile from ESP model has the same fluctuating trend with the exact solution from P2D model, but the deviation is a little large. As for the battery with parameters in Table 3 simulated in this work, the maximum C-rate that ESP model can predict with a good accuracy is 4C. Further improving the maximum C-rate should improve the approximate description accuracy in ESP model. For example, the number of the selected typical active particles used in the approximate solution in Section 3.2.4 could be improved from three to five, and the exponential function which describes the open circuit potential distribution should be adjusted accordingly, but these adjustments will increase the complexity and the computation cost of the model.

Secondly, the terminal voltage results under different C-rates are plotted and compared in Fig. 10.

From Fig. 10 it can be concluded that, under the galvanostatic discharges with different C-rates up to 4C, ESP model can accurately simulate the terminal voltage profiles. The deviations between the results from ESP model and P2D model are small and distribute around the zero point. Correspondingly, the deviations of SP model are all positive errors under discharge and increase with the increase of the discharge C-rates.

4.3. The accuracy of ESP model

In order to illustrate the accuracy of ESP model more clearly, the root-mean-square errors (RMSEs) are calculated to measure the differences between the terminal voltage profiles predicted by ESP/SP model and those from P2D model. The RMSEs of ESP and SP model under different operating conditions are plotted in Fig. 11.

Analyzing the RMSEs under different C-rate galvanostatic discharges from 1C to 4C, it can be seen that, the deviations of both the ESP model and SP model increase with the increase of the discharge C-rates. Under all the test operating conditions, the RMSEs of ESP model are significantly lower than that of SP model. In detail, the RMSEs of ESP model are 4.4 mV/8.7 mV/11.4 mV/19.9 mV for 1C/2C/3C/4C rate discharges respectively, which are only 19% of the corresponding RMSEs of SP model. Therefore, the accuracy of ESP model improves significantly compared with the SP model. This conclusion can also be arrived at in the other three operating conditions in Fig. 11: the constant current constant voltage (CCCV) charge, the Dynamic Stress Test (DST) discharge and the Federal Urban Driving Schedule (FUDS) discharge. Then, with respect to the platform voltage 3.6 V of Lithium-ion batteries, the relative errors of ESP model are 0.12% at 1C rate discharge, 0.24% at 2C rate discharge, 0.32% at 3C rate discharge and 0.55% at 4C rate discharge. Therefore, ESP model is an effective approximate physics-based lithium-ion cell model with a good accuracy. It can be applied up to 4C rate charge–discharge operating conditions with an average relative error less than 0.55%.

4.4. Charge and dynamic operating conditions

Additionally, ESP model can be applied to arbitrary loads composed of charge/discharge or interval, constant current or pulse, as well as the dynamic loads. For validation, the CCCV charge, the DST and FUDS discharge are carried out as three test operating conditions. DST and FUDS are two variable power discharge regimes defined for United States Advanced Battery Consortium (USABC) testing of the EV and HEV batteries. The results are illustrated in Fig. 12.

Table 4
The simulation times of SP ESP and P2D models.

Operating conditions	SP	ESP	P2D	Ratio (ESP/P2D)	Ratio (ESP/SP)
1C discharge	0.758 ms	10.55 ms	11.15 s	1/1057	13.9
2C discharge	1.421 ms	15.56 ms	16.85 s	1/1083	11.0
3C discharge	4.534 ms	56.31 ms	59.18 s	1/1051	12.4
4C discharge	6.777 ms	91.09 ms	94.34 s	1/1036	13.4
0.5C CCCV charge	2.901 ms	33.61 ms	31.75 s	1/945	11.6
4C DST	1.601 ms	22.08 ms	19.91 s	1/902	13.8
4C FUDS	35.247 ms	527.43 ms	530.77 s	1/1006	14.9

From Fig. 12b it can be seen that the deviations of SP model are positive under discharge and negative under charge. Compared with the SP model, the deviations of ESP model are smaller and distribute around the zero point. Comparison of the result profiles in Fig. 12c–f under DST and FUDS discharges also confirms the conclusion that ESP model can be applied to dynamic loads and the accuracy is significantly better than SP model.

4.5. The computational efficiency

Analyzing the corresponding equations, it can be seen that ESP model is a lumped-parameter analytical model. A key advantage of this analytical model is that it uses an algorithmic procedure without repeated numerical simulations (such as the finite difference method). Therefore, compared with the original physics-based P2D model, ESP model will greatly improve the computational efficiency. The simulation times of SP ESP and P2D models under different operating conditions are compared, and the results are listed in Table 4.

The following results can be concluded from Table 4. Corresponding to the different complexities of different operating conditions, the simulation time of SP model is between one millisecond to tens of milliseconds. The simulation time of ESP model is between ten milliseconds to hundreds of milliseconds, and that of P2D model is between ten seconds to hundreds of seconds. In terms of the simulation times of the three models, that of ESP model is one thousandth of P2D model and thirteen times of SP model on average. Therefore, ESP model greatly improves the computational efficiency compared with the original P2D model.

5. Conclusions

A new approximate physics-based Lithium-ion cell model ESP is developed by extending the descriptions of the non-uniform reaction distribution effect and the electrolyte concentration/potential distribution effect into SP model. ESP model can accurately predict the pore wall fluxes at the two current collector interfaces. It addresses the key issue that SP model is not valid for higher charge–discharge rates. The following conclusions are obtained through comparing ESP model with the original P2D model.

Firstly, ESP model can be applied to higher charge–discharge rates up to 4C with a relative error less than 0.55%.

Secondly, ESP model can be applied to arbitrary loads composed of charge/discharge or interval, constant current or pulse, as well as the dynamic loads.

Thirdly, ESP model is a lumped-parameter analytical model with a good computational efficiency. Under the same configuration, the simulation time of ESP model is only one thousandth of P2D model. It is suitable for the real-time simulation embedded in a microprocessor in the EV and HEV applications.

Acknowledgments

The authors are thankful for the financial support of this work provided by the Natural Nature Science Foundation of China: NSFC 51107021, and the Fundamental Research Funds for the Central Universities (Grant No. HIT. NSRIF. 2014021). We thank Prof. Kedong Liu who provides language help.

References

[1] V. Ramadesigan, P.W.C. Northrop, S. De, S. Santhanagopalan, R.D. Braatz, V.R. Subramanian, Journal of The Electrochemical Society 159 (2012) R31–R45.
[2] A.P. Schmidt, M. Bitzer, A.W. Imre, L. Guzzella, Journal of Power Sources 195 (2010) 5071–5080.
[3] V.R. Subramanian, V.D. Diwakar, D. Tapriyal, Journal of The Electrochemical Society 152 (2005) A2002–A2008.
[4] M. Guo, G. Sikha, R.E. White, Journal of The Electrochemical Society 158 (2011) A122–A132.
[5] V. Ramadesigan, V. Boovaragavan, J.J.C. Pirkle, V.R. Subramanian, Journal of The Electrochemical Society 157 (2010) A854–A860.
[6] Q. Zhang, R.E. White, Journal of Power Sources 165 (2007) 880–886.
[7] P.W.C. Northrop, V. Ramadesigan, S. De, V.R. Subramanian, Journal of The Electrochemical Society 158 (2011) A1461–A1477.
[8] V.R. Subramanian, V. Boovaragavan, V. Ramadesigan, M. Arabandi, Journal of The Electrochemical Society 156 (2009) A260–A271.
[9] V. Boovaragavan, S. Harinipriya, V.R. Subramanian, Journal of Power Sources 183 (2008) 361–365.
[10] S.K. Rahimian, S. Rayman, R.E. White, Journal of Power Sources 196 (2011) 8450–8462.
[11] W. Luo, C. Lyu, L. Wang, L. Zhang, Microelectronics Reliability (2012). http://dx.doi.org/10.1016/j.microrel.2012.11.002.
[12] J. Newman, K.E. Thomas-Alyea, Electrochemical Systems, third ed., Wiley-Interscience, Hoboken, NJ, 2004.
[13] M. Doyle, T.F. Fuller, J. Newman, Journal of The Electrochemical Society 140 (1993) 1526–1533.
[14] M. Doyle, J. Newman, A.S. Gozdz, C.N. Schmutz, J.-M. Tarascon, Journal of The Electrochemical Society 143 (1996) 1890–1903.
[15] T.-S. Dao, C.P. Vyasarayani, J. McPhee, Journal of Power Sources, 198 329–337.
[16] T.F. Fuller, M. Doyle, J. Newman, Journal of The Electrochemical Society 141 (1994) 1–10.
[17] D. Zhang, B.N. Popov, R.E. White, Journal of The Electrochemical Society 147 (2000) 831–838.
[18] S. Santhanagopalan, Q. Guo, P. Ramadass, R.E. White, Journal of Power Sources 156 (2006) 620–628.